Microtearing modes as the source of magnetic fluctuations in the JET pedestal

D. R. Hatch[1*], M. Kotschenreuther[1], S. M. Mahajan[1], M. J. Pueschel[1], C. Michoski[2], G. Merlo[2], E. Hassan[1], A. R. Field[3], L. Frassinetti[4], C. Giroud[3], J. C. Hillesheim[3], C. F. Maggi[3], C. Perez von Thun[5], C. M. Roach[3], S. Saarelma[3], D. Jarema[6], F. Jenko[1,2,6], JET contributors[7]

[1]Institute for Fusion Studies, University of Texas at Austin, Austin, Texas, 78712
[2]Oden Institute for Computational Engineering and Sciences, University of Texas at Austin, Austin, Texas, 78712
[3]CCFE, Culham Science Center, Abingdon OX14 3DB, United Kingdom
[4]Division of Fusion Plasma Physics, KTH Royal Institute of Technology, SE-10691 Stockholm, Sweden
[5]Institute of Plasma Physics and Laser Microfusion, Hery 23, 01-497 Warsaw, Poland
[6]Max-Planck-Institute for Plasma Physics, Boltzmannstrasse 2, 85748 Garching, Germany
[7]See the author list of E. Joffrin *et al.* 2019 Nucl. Fusion 59 112021

E-mail: *drhatch@austin.utexas.edu

Abstract.

We report on a detailed study of magnetic fluctuations in the JET pedestal, employing basic theoretical considerations, gyrokinetic simulations, and experimental fluctuation data to establish the physical basis for their origin, role, and distinctive characteristics. We demonstrate quantitative agreement between gyrokinetic simulations of microtearing modes (MTMs) and two magnetic frequency bands with corresponding toroidal mode numbers n=4 and 8. Such disparate fluctuation scales, with substantial gaps between toroidal mode numbers, are commonly observed in pedestal fluctuations. Here we provide a clear explanation, namely the alignment of the relevant rational surfaces (and not others) with the peak in the ω_* profile, which is localized in the steep gradient region of the pedestal. We demonstrate that a global treatment is required to capture this effect. Nonlinear simulations suggest that the MTM fluctuations produce experimentally-relevant transport levels and saturate by relaxing the background electron temperature gradient, slightly downshifting the fluctuation frequencies from the linear predictions. Scans in collisionality are compared with a simple MTM dispersion relation. At the experimental points considered, MTM growth rates can either increase or decrease with collision frequency depending on the parameters thus defying any simple characterization of collisionality dependence.

PACS numbers: 00.00

1. Introduction

High frequency magnetic fluctuations are often observed in the edge of H-mode discharges[1, 2, 3, 4, 5, 6, 7]. On JET, these fluctuations have been dubbed washboard modes [1] due to their distinctive appearance in magnetic spectrograms and in lieu of a clearly identified underlying physical mechanism. These fluctuations are localized in or near the pedestal; arise during the inter-ELM cycle; are correlated with the saturation of pedestal temperature (in contrast with density); and have frequencies in the electron diamagnetic direction [1]. In this paper, we study such fluctuations using basic theoretical considerations along with gyrokinetic simulations using the GENE code [8, 9] (genecode.org) and unambiguously identify them as microtearing modes (MTMs), thus establishing an increasingly firm physical basis for their origin, role, and distinctive characteristics.

The microtearing mode was first described in Ref. [10], which established already the central characteristics of the basic instability: its intrinsic electromagnetic nature, a reliance on mode frequency being roughly comparable to the collision frequency, its drive by the electron temperature gradient, and a frequency close to $\omega_{e*} = k_y \rho_s c_s (1/L_n + 1/L_{Te})$ (here, k_y is the binormal wavenumber, ρ_s is the sound gyroradius, c_s is the sound speed, and $L_{n,Te}$ is the gradient scale length of the density or temperature). Subsequent work [11, 12] elucidated the role of the parallel wavenumber, $k_{||}$, the separate influence of density and temperature gradients, and the possibility of collisionless variations on the theme [13, 14, 15, 16]. Gyrokinetic simulations have further explored the nonlinear saturation physics [17, 18, 19], and its role in spherical tokamaks (both core [20, 19, 21], and edge [22, 23]). In an interesting recent development, Ref. [24] identifies MTM as the electron heat transport mechanism in an internal transport barrier on DIII-D, thus establishing a unifying connection with the present work: the activity of MTM in transport barriers after the conventional turbulent transport mechanisms have been suppressed.

This paper builds on a series of recent papers that demonstrate that MTM is a prominent fluctuation in the steep gradient region of the pedestal [25, 26]. Ref. [25] identified MTM as the salient ion-scale instability in a JET ITER-like wall (JET-ILW) discharge, noted its unusual mode structure (peaking at the top and bottom of the tokamak), and demonstrated that nonlinear simulations can reproduce experimental transport levels. Ref. [26] argued that MTMs are likely responsible for pedestal transport on many discharges based on their distinctive physical characteristics, placed MTMs among other prospective pedestal transport mechanisms, and demonstrated close correspondence between GK simulations and magnetic spectrograms for two DIII-D discharges. Recently, experimental work has exploited an innovative measurement of internal magnetic fluctuations [27] to further establish MTM as a common pedestal fluctuation in DIII-D [6].

This paper expands this line of research in several ways: (1) demonstrating quantitative agreement between GK simulations and distinctive features of magnetic

spectrograms, namely discrete bands of frequencies at disparate toroidal mode numbers, n (Sec. 3); (2) providing a clear explanation for the discrete band structure (Sec. 4); (3) elucidating the underlying physics by comparing MTM collisionality dependence with a simple dispersion relation (Sec. 4.2); (4) demonstrating that global simulations are necessary to quantitatively reproduce the experimental fluctuations (Sec. 4.1); (5) elucidating a possible nonlinear saturation mechanism and demonstrating experimentally realistic transport levels (Sec. 5); and (6) discussing the role of MTM in limiting the pedestal and influencing inter-ELM pedestal evolution (Sec. 6).

2. Magnetic Fluctuations in JET pulse 78697

JET pulse 78697 is a high current, high field (3 MA, 2.4 T) carbon wall discharge characterized by parameters shown in Table 1 and profiles shown in Fig. 1. It was examined in detail in a comparative study of pedestal transport on JET [28], for which it was selected as a carbon wall counterpart to a high-performance JET discharge (pulse 92432) from the ITER-like wall (ILW) period. MTMs were also studied in an additional JET discharge (pulse 82585) as reported in Ref. [25]. This paper focuses mostly on pulse 78697, for which we have carried out a detailed comparison with magnetic fluctuation measurements. Some results from 82585 will also be discussed. Pedestal profiles of electron temperature and density are shown in Fig. 1. The uncertainty band shown in Fig. 1 is calculated using a simple Monte Carlo method. One thousand modified tanh functions were created with different input parameters. The input parameters are determined from the average plus a random value sampled from a Gaussian distribution centered at 0 and with one standard deviation uncertainty in the parameters. The upper and lower bounds in the figure highlight the region within one standard deviation.

2.1. Magnetic Fluctuation Data

Mirnov coils on JET often identify magnetic fluctuations, so-called washboard modes, with distinct frequency bands [1]. Ref. [1] determined that these fluctuations are localized in or near the pedestal; arise during the inter-ELM cycle; are correlated with the saturation of pedestal temperature (in contrast with density); and have frequencies in the electron diamagnetic direction. All these properties are consistent with the MTM, which is reinforced by the simulation results described below.

Fig. 2 shows the magnetic spectrogram for JET pulse 78697. The color denotes the toroidal mode numbers extracted from the phase shift of the signal from a toroidal set of Mirnov coils (the sign indicates electron [negative] and ion [positive] diamagnetic direction). The low frequency (green) bands are core modes that are not correlated with the inter-ELM cycle and not of interest for the present study. We are interested, rather, in the high frequency bands propagating in the electron diamagnetic direction (blue). Four inter-ELM cycles are captured in Fig. 2. Here, we focus on the two middle cycles in the time range $t \sim 50.4s - 50.55s$, which exhibit slightly different frequency bands

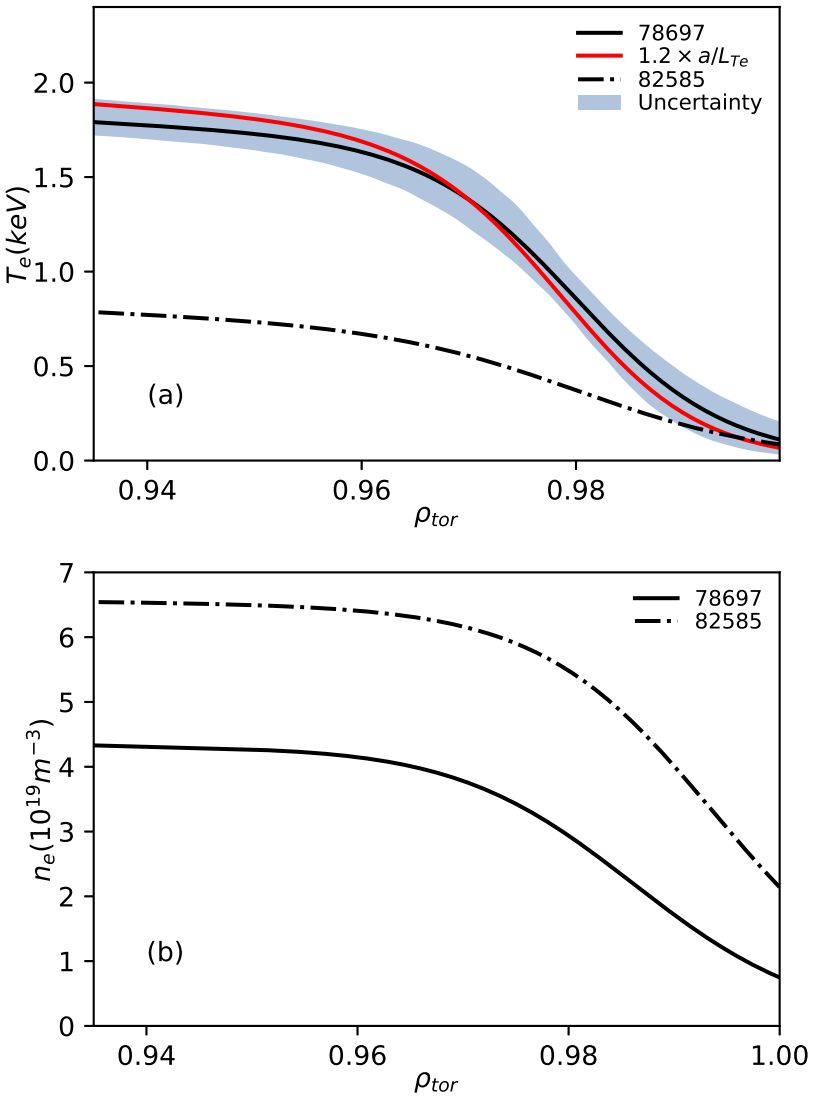

Figure 1. Profiles of electron temperature (top) and electron density (bottom) for two JET discharges. The shaded band around the 78697 T_e profile signifies the $\pm 1\sigma$ uncertainty in the profile and the red line is an additional T_e profile (within the uncertainty band) used for some simulations.

from the first and last inter-ELM cycles. At least two distinct bands are manifest: a lower frequency band ($f \approx 60 - 80kHz$) with dominant contributions from $n \sim -4, -5$ and a higher frequency band ($f \sim 100 - 140kHz$) with dominant contributions from $n \approx -7, -8, -9$. This can be viewed, roughly, as two bands at $n = -4 \pm 1$ and $n = -8 \pm 1$. As will be described below, gyrokinetic simulations produce MTMs with these characteristics.

In order to compare simulations with these lab-frame measurements, the rotation must be carefully accounted for. Direct measurements of the radial electric field E_r and parallel flow $V_{||}$ were not available for this discharge. Consequently, we estimate E_r

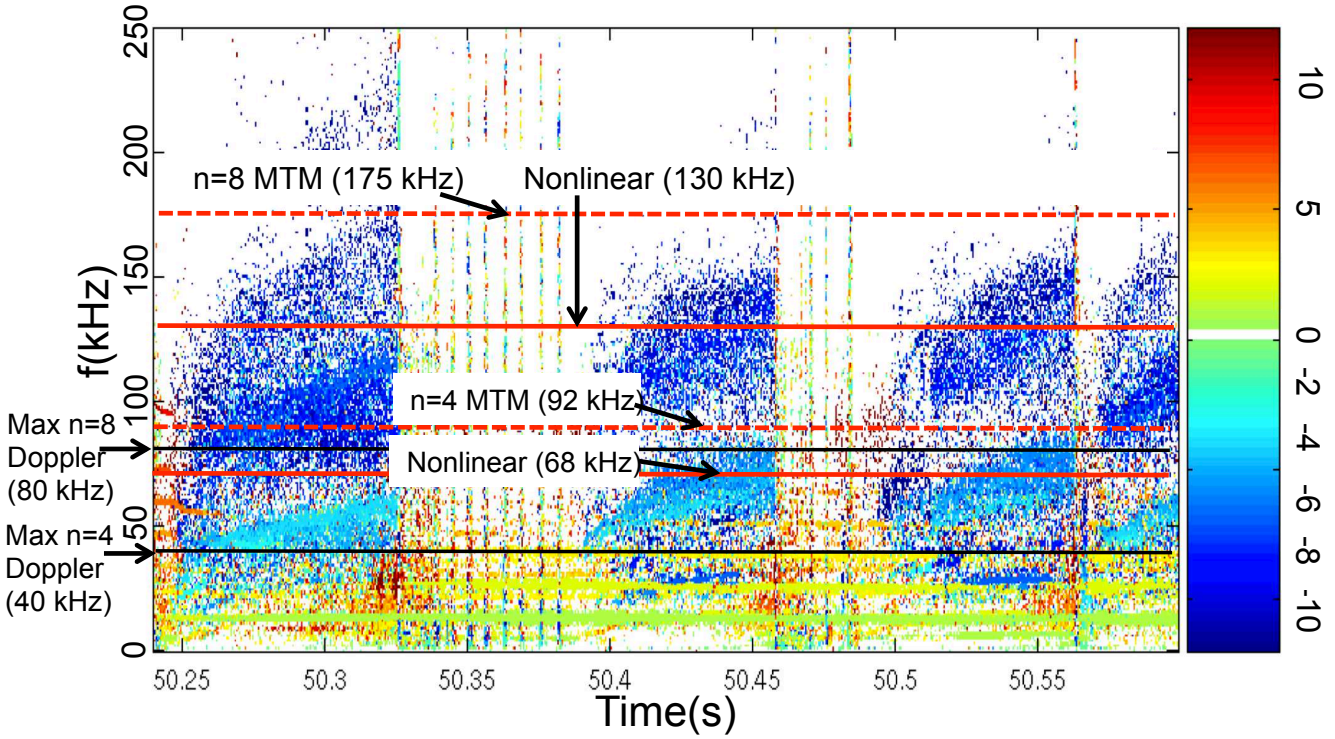

Figure 2. Magnetic spectrogram for JET-C (78697) showing frequency bands and toroidal mode numbers of magnetic fluctuations. The color denotes the toroidal mode number, and the sign of the toroidal mode number denotes the propagation direction (negative—electron diamagnetic). The blue high frequency bands correspond to washboard modes and are the focus of this paper. We focus, in particular on the two central inter-ELM periods ($t(s) = 50.4-50.55$) The abrupt cessations of the washboard fluctuations correspond to ELM crashes. The green lower frequency bands denote core modes, which are not correlated with the inter-ELM behavior and not of interest in this paper. The dashed lines denote the frequencies of MTMs from global gyrokinetic simulations carried out in the lab frame ($n = 8$ at $\sim 174kHz$, and $n = 4$ at $92kHz$). The lower solid red lines show frequencies from nonlinear simulations. The maximum Doppler shifts (black) from $E_r \times B$ rotation are shown in black, demonstrating that the washboard modes are propagating in the electron direction in the plasma frame.

using the standard neoclassical formula [29],

$$V_{||} = -\frac{RB_\phi}{ZeB}\left(\frac{1}{n_i}\frac{dP_i}{d\psi} + Ze\frac{d\Phi_0}{d\psi} - K\frac{B^2}{< B >^2}\frac{dT_i}{d\psi}\right). \quad (1)$$

where $V_{||}$ is the parallel flow, R is the major radius, B_ϕ is the poloidal magnetic field, P_i is the ion pressure, Φ_0 is the electrostatic potential, and ψ is the normalized poloidal magnetic flux (readers are referred to Ref. [29] for more detailed definitions, e.g., of K). Since there is no measurement available, we use the approximation $V_{||} = 0$, which is justified by the fact that in other pedestal scenarios where measurements are available, the dominant balance in Eq. 1 is between the radial electric field and the gradients [30]. Note that the Doppler shift in the pedestal is in the electron diamagnetic direction and thus opposite to that of the bulk plasma rotation in the core, so the inclusion of $V_{||}$ would be expected to slightly decrease the net Doppler shift. The resulting $E \times B$ advection from the radial electric field is included in the simulations described below so that the simulations are carried out in the lab frame. The resulting Doppler shift is $\Omega = \frac{nE_r}{RB_\theta}$. A detailed discussion of the Doppler shift is provided in Appendix A.

The maximum (over radial location) Doppler shifted frequency is a useful discriminator between ion frequency fluctuations, like kinetic ballooning modes (KBMs), and fluctuations with frequencies strongly in the electron direction, like MTMs. These maximum Doppler frequencies, shown in Fig. 2 for $n = 4, 8$ lie at the lower bound of the measured frequencies of the washboard fluctuations in the first inter-ELM cycle and well below the measured frequencies for the other ELM cycles. This is a clear indication that the fluctuations are propagating in the electron diamagnetic direction in the plasma frame.

We also note in passing an additional narrower band with $n = -7$, which is observed in the second and third ELM cycles with $f \sim 30kHz$. This frequency is far below the corresponding $n = 7$ Doppler shift. Possible explanations include (1) a MTM localized at the pedestal top where both the Doppler shift and ω_{e*} are much smaller (note that pedestal-top MTMs have been described in Ref. [22, 31, 32, 21]), and (2) a KBM or ITG mode with ion frequency in the plasma frame.

3. Comparison between Linear Simulations and Spectrograms

Global linear simulations for JET discharge 78697 were performed with minor modifications to the simulation inputs to test sensitivities. The toroidal mode number n is directly proportional to the binormal wavenumber, k_y, so that each solution of the linear eigenvalue problem corresponds to a single n. In contrast, the resulting eigenmode encompasses several poloidal m numbers. Numerical details are described in Appendix C. Two cases will be discussed in detail: (1) the base case comprising the nominal profiles and equilibrium reconstruction, and (2) a scenario (labeled 'Mod 1') with a 5% reduction in safety factor q and a 20% increase in the electron temperature gradient (maintaining constant total pressure by decreasing the ion temperature gradient correspondingly). The relevance of the modified q profile will be discussed below. The 20% increase in electron temperature gradient is within the error bars of the experimental measurement as shown in Fig. 1. Likewise, the minor variation of the q profile is also likely within experimental uncertainty.

Fig. 3 shows growth rates (left) and frequencies (right) for these two cases: the Base case in black and Mod 1 in red. MTMs are denoted with circles and other modes with plus symbols. For the base case, MTMs are observed at $n = 8, 9$ (in agreement with the spectrogram) but not at $n = 4$. The instability that is found at $n = 4$ does not correspond to the observed fluctuations, having a much lower frequency.

For the Mod 1 case, MTMs are unstable at $n = 4, 8, 9$, in quantitative agreement with the experimental observation, whose range in the spectrogram is denoted by the shaded blue regions. Likewise, there is reasonable agreement between simulated and observed frequencies, with the simulated frequencies surpassing the observed frequencies by $\sim 30\%$. Quantitative agreement is achieved in nonlinear simulations, which will be described in Sec. 7. Notably, the most distinctive feature of the spectrograms—the quasi-coherent bands at disparate n numbers—is reproduced by the simulations in the sense that unstable MTMs are observed at toroidal mode numbers $n = 4, 8, 9$ but not those in between ($n = 5, 6, 7$). The underlying mechanism for this distinctive behavior is elucidated in the next subsection. We also note that, although the $n = 12$ mode is unstable in the simulations, it is not idenfied in the spectrogram. Plausible explanations include (1) the weaker growth rate and stronger nonlinear stabilization at higher n; (2) the fact that a higher m perturbation will decay much more rapidly before reaching the external Mirnov coils and so may not be detected; and (3) the inherent uncertainties in the background profiles.

For reference, results from local MTM simulations for the Mod 1 case located at the peak in the global mode structure—$\rho_{tor} = 0.978$—are shown in Fig. 3 in gray. They exhibit similar growth rates to the global simulations only at mode numbers where MTMs are strongly unstable in the global simulations. Notably, inconsistent with the experimental observations, the local growth rates also exhibit instability at the intermediate n numbers. Local simulations are discussed further in Sec. 4.1, where it is concluded that the local approach is inadequate for capturing the distinctive features of pedestal MTMs and, moreover, can be quite misleading for this scenario.

4. Explanation for frequency bands

Perhaps the most important result of this work is a clear explanation for the distinct fluctuation bands at disparate n numbers. The key insight follows from a careful examination of the alignment of the MTM drive, i.e. $\omega_{e*} = k_y \rho_s c_s (1/L_n + 1/L_{Te})$ with the relevant rational q surfaces, as shown in Fig. 4. In this figure, the ω_{e*} profile (black) is shown along with the q profile (blue) and representative linear eigenmode structures (dashed blue). Vertical lines denote rational surfaces, labeled with their respective toroidal and poloidal mode numbers. Fig. 4 A. shows the base case, where $(n, m) = (8, 23)$ and $(n, m) = (9, 26)$ are the surfaces that align most closely with the peak in the ω_{e*} profile, corresponding to the unstable MTM at $n = 8, 9$ (recall Fig. 3). Notably, the $n = 4$ rational surfaces lie far from the peak in ω_{e*} and there is no $n = 4$ instability that corresponds to the fluctuation data. In contrast, Fig. 4 B. shows results

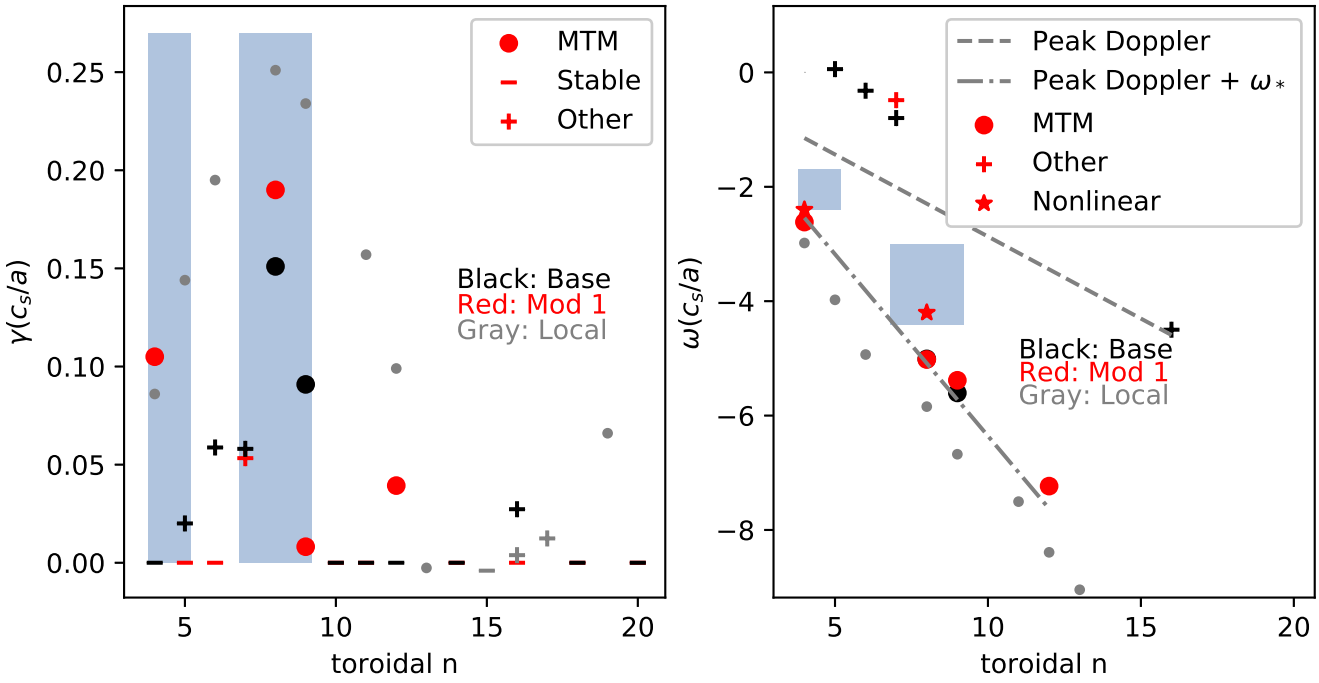

Figure 3. Growth rates and frequencies from gyrokinetic simulations for two cases. The base case uses the nominal experimental inputs and the Mod 1 case uses a slightly shifted q profile and a 20% increase in the electron temperature gradient (shown in Fig. 1). The circles denote MTMs and the plus symbols denote other modes. The blue shaded regions signify the experimental values from the magnetic spectrogram. The red stars denote the frequencies calculated in a nonlinear simulation. The MTMs from the Mod 1 case agree quantitatively with the toroidal mode numbers and frequencies observed in the spectrogram.

for the Mod 1 case (differing in a $\sim 5\%$ decrease in the q profile). In this case, the $(n, m) = (4, 11)$ and $(n, m) = (8, 22)$ rational surfaces now both align with the peak in ω_{e*}, resulting in unstable mode numbers that correspond quantitatively with the magnetic spectrogram. We thus have a clear explanation for the discrete frequency bands observed in the data, namely the alignment of particular rational surfaces with the peak in the ω_* profile.

The possible cause of the sensitive n number selection, and the mode localization near the ω_* peak could be traced to two essential processes responsible for the eigenmode formation:

1) The best condition for existence, i.e, the close proximity of the rational surface and ω_* peak, is precisely the desired condition for the largest growth rate; gradient free energy is maximum in the region of localization.

2) The standard "potential well" in which the MTM lives (when pressure gradients are neglected) is created by magnetic shear; in the pedestal, however, the strong variation of ω_* can seriously modify this confining well. The proximity of the rational

surface near the ω_* peak seems to ensure the possibility of instability. A detailed analytic analysis of these physical considerations is currently being pursued and will be published elsewhere.

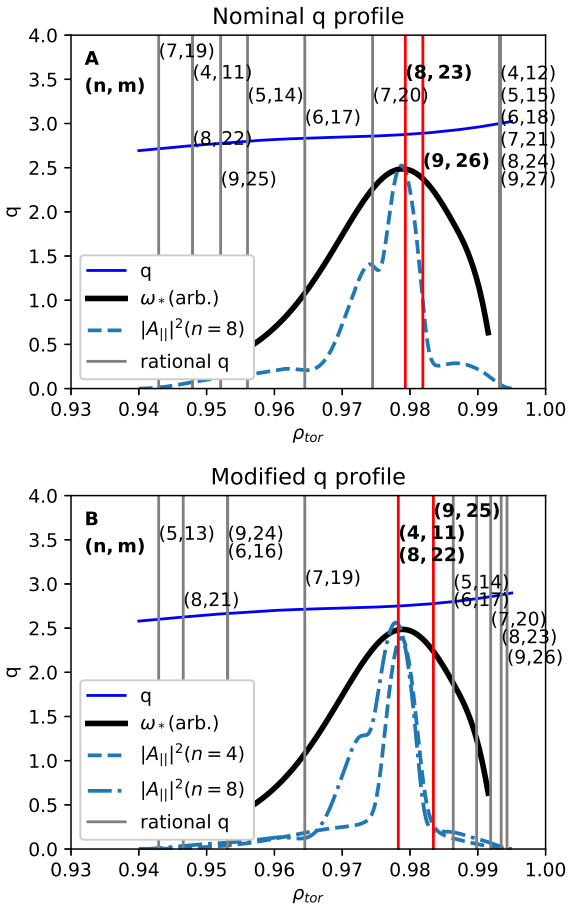

Figure 4. q profiles, ω_* profiles, and MTM mode structures for the Base and Mod 1 cases. The vertical lines correspond to rational surfaces and are labeled by their corresponding n and m numbers. For the Base case, simulations find unstable MTMs only at $n = 8, 9$. For the Mod 1 case $n = 4, 8, 9$ are found to be unstable in agreement with the experimental observations. An MTM is unstable at a given n only when the respective rational surface align with the peak in the ω_* profile, providing an explanation for the bands observed in the spectrogram.

4.1. Local vs. Global

Local simulations were carried out centered at the radial location where the global modes peak ($\rho_{tor} = 0.978$). As described in Ref. [25], MTMs can be unstable at finite θ_0, requiring a scan of this dimension in the local simulations. Growth rates and frequencies are shown in Fig. 5. A strongly unstable MHD-like mode exists at this radial location as denoted with the black symbols. The frequencies for these modes are unconventional in that they are negative at low n and transition to positive as n increase. The mode

structure of the low n modes, together with the fact that the mode disappears when ion temperature gradients are eliminated, is suggestive of past descriptions of ideal MHD modes that are destabilized below the ideal threshold by kinetic effects arising at large ballooning angle. The tail of this mode has a long decaying envelope in theta, with oscillations of 2π, similar to these. The modes in the early literature [33, 34, 35] have positive mode frequency (ion direction) but are also described in circular geometry, and it is possible that strongly shaped geometry (i.e., near the separatrix) could lead to a negative frequency. These modes are more difficult to destabilize when the ideal MHD mode is further below marginal stability. This might also explain why these modes disappear in global calculations—the ideal ballooning mode is more stable in such global calculations as described in Refs. [25, 26, 28]. This phenomenon was explained by noting that the effective radial extent of the local modes (dominated by $k_x = 0$) is inconsistent with the physical extent of its instability drive, which is limited to the steep gradient region of the pedestal (readers are referred to Refs. [26, 28] for further discussion and a criterion for when this phenomenon may be expected to occur). In addition to their stability in the global simulations, the experimental data also is inconsistent with the characteristics of these modes: (1) the frequency of the $n = 4$ mode is roughly in the right range, but the trend in the dispersion relation is opposite that of the experimental observation so that the $n = 8$ frequency is incorrect, and (2) the modes are unstable at each consecutive n as opposed to the distinct and separated n numbers observed in global simulations of MTMs. We conclude that, for the purpose of explaining the experimental characteristics, the focus on MTMs in the previous sections is justified and a global treatment is likely necessary to quantitatively reproduce the observations.

The subdominant MTM instabilities can be identified either by considering higher θ_0 (denoted by red dots in Fig. 5) or by eliminating the ion temperature gradient (red x symbols), which stabilizes the fastest growing mode while leaving the MTMs unchanged. As noted above in the discussion of Fig. 3, the local MTMs have roughly the same growth rates as the global calculations for $n = 4, 8$. However, in contrast with global, the local MTMs exhibit a smooth dispersion relation, with instabilities at each consecutive n. This is easily explained by noting that (1) in a local treatment, ω_* is defined by its local value and (2) the q profile is linear (i.e. has constant $\hat{s}$). Consequently, different n numbers whose rational surfaces may be slightly offset from each other still sample the same value of ω_*, in contrast with the global treatment (recall Fig. 4).

We conclude that the local approximation is inadequate for quantitatively reproducing the observed magnetic fluctuations and, moreover, may produce artificially unstable MHD modes. It remains to be seen whether alternative approaches to capturing nonlocal effects [36, 37] would be sufficient. The present scenario would be a compelling test of such approaches.

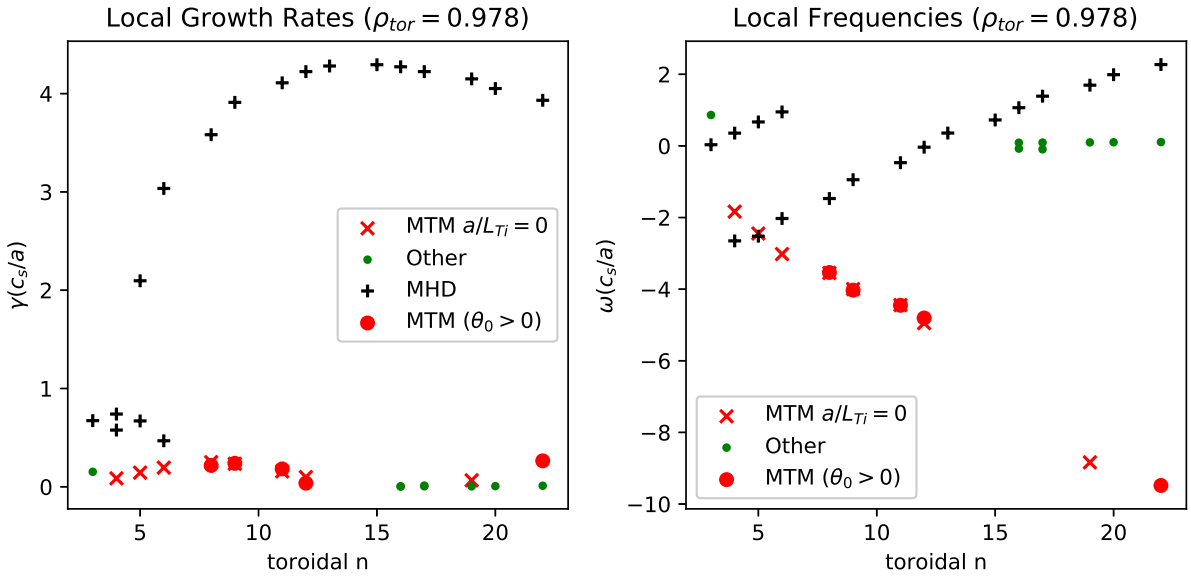

Figure 5. Growth rates and frequencies from local linear simulations.

Table 1. Summary of important parameters for JET pulse 78697 (C). I_p is the plasma current, B_T is the toroidal magnetic field, q_{95} is the safety factor at 95% of the minor radius (in terms of normalized poloidal magnetic flux), δ is triangularity, P_h is the total heating power, P_i is the inter-ELM power loss [38], Gas is the fueling rate, β_N is normalized plasma pressure, $T_{e,p}$ is the pedestal top electron temperature, and $n_{e,p}$ is the pedestal top electron density.

Pulse	$I_p(MA)$	$B_T(T)$	q_{95}	δ	$P_h(MW)$	$P_i(MW)$	Gas(e/s)	β_N	$T_{e,p}(keV)$	$n_{e,p}(10^{19}$
78697	3.0	2.4	2.6	0.24	14.8	5.7	0.0	1.8	1.68	4.19

4.2. Simple MTM Dispersion Relation

In order to elucidate the underlying physics and further establish the modes of interest as MTMs, we make comparisons with the simple MTM dispersion relation from Ref. [10]

$$(\nu - 0.54i\omega)\,(\omega - \omega_{e*}) - 0.8\omega_{T*}\nu = 0, \tag{2}$$

where ν is the electron collision frequency, $\omega_{e*} = k_y\rho_s c_s(1/L_n + 1/L_{Te})$, and $\omega_{T*} = k_y\rho_s c_s(1/L_{Te})$. More sophisticated versions are currently being studied and comparisons will be published elsewhere. Fig. 6 shows the solution to this dispersion relation along with simulated collisionality scans (holding all other parameters fixed) for both 78697 and 82585 for various n numbers using both local and global modes of operation. We focus first on the black and red symbols corresponding to the $n = 4, 8$ modes, respectively, for JET pulse 78697. Although the simple dispersion relation differs substantially from the simulation results in the magnitude of the growth rate, it quantitatively captures the collisionality threshold and qualitatively captures other

major features of the collisionality dependence, including a peak in growth rate at $\nu \sim \omega$ and subsequent falloff of growth rates at higher frequency. This demonstration, in combination with other features of the mode, including predominantly electromagnetic heat flux, intrinsic electromagnetic nature (does not exist in the electrostatic limit), a large component of tearing parity, $\omega = \omega_{e*}$, and very weak dependence on kinetic ions, unambiguously identifies the modes as MTMs. Investigations of more comprehensive dispersion relations, which include η (ratio of density gradient scale length to temperature gradient scale length) effects, finite $k_{||}$ effects, and more sophisticated conductivity [39] are currently being undertaken and will be published elsewhere. Additionally, the dispersion relation in Ref. [40], which additionally captures curvature effects, is likely to find improved agreement with the simulation results. We leave such investigations for future work.

We briefly comment on the collisionality scans for 82585, which exhibit a tail in the collisionless limit. Extensive tests were conducted in this low collisionality regime and the mode persists with (nearly) the same growth rate even with doubled velocity space resolution, zero collisionality, zero hyperdiffusion, and a conservative numerical scheme (Arakawa). We speculate that these modes retain some instability drive through a toroidal (curvature) resonance. Such variations in MTM physics appear to be responsible for the multiple bands that are observed in some discharges. For example, DIII-D discharge 162940 exhibits three distinct frequency bands: narrow bands at 40 kHz, 80 kHz, and a broader band centered at 400 kHz, which are in quantitative agreement with simulations as described in Ref. [41].

We also note the plus symbols in Fig. 6, which correspond to the experimental values of collisionality. The experimental points lie firmly in the range where the collisional effects are active. In most of these cases, the experimental points lie below the peak of the dispersion relation, indicating that generally higher collisionality will destabilize the mode. However, for the global simulation of discharge 82585, collisionality is clearly stabilizing, suggesting that the collisionality dependence may not be so easily characterized. Similarly to Fig. 6, Table 2 of Ref. [26] showed that the frequency of observed magnetic fluctuations of several discharges on ASDEX, DIIID and JET was consistent with MTM destabilization as in Eq. 2, suggesting that the physics simulated here applies to a wide class of pedestals.

5. Nonlinear Simulations

Although the global nonlinear simulations described here offer several physical insights, they should be considered to be a qualitative representation of the dynamics due to certain numerical limitations. The two main limitations are (1) numerical instabilities that preclude long-time simulations and extensive convergence tests, and (2) the artificial nature of the sources used to maintain the background profiles in gradient-driven simulations. Solutions to both of these limitations are actively being developed by the GENE development team. Despite these limitations, several valuable insights can

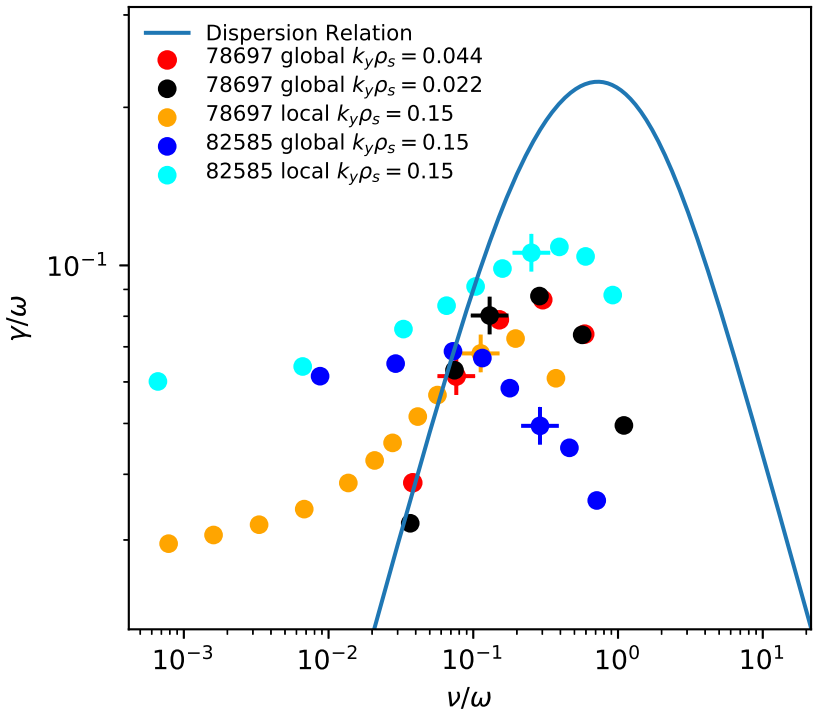

Figure 6. Comparisons between collisionality scans for various k_y modes in two JET discharges and a simple MTM dispersion relation. The simple dispersion relation qualitatively captures some of the collisionality dependence of the MTM. In three of the cases, a collisionless tail is observed. However, the experimental points (plus symbols) all correspond to a collisional or semi-collisional regime.

be gained.

In order to simplify the dynamics, an adiabatic ion assumption is used, which results in minor quantitative changes for MTM stability (approximately 30% reduction in growth rates). In light of the above discussion, global simulations are necessary to capture the relevant physics. As a first step, we retained only three toroidal mode numbers, $n = 0$ along with the two mode numbers that appear most-prominently in the magnetic spectrogram: $n = 4, 8$. Time traces for the electromagnetic heat flux are shown in Fig. 7 A. for the base case simulation (black) and the Mod 1 case (blue). As a convergence test, six toroidal mode numbers are used for the Mod 1 case, ($n = 0, 2, 4, 6, 8, 10$), exhibiting only minor quantitative differences with the three mode simulation. This simulation (six toroidal mode numbers) is the focus of the main results described below. Background $E \times B$ shear is included in all nonlinear simulations. Additional numerical details, including details on hyperdiffusion and source rates, are reported in Appendix C.

In gradient-driven global simulations, source terms (Krook operators with time-independent coefficients) are employed in order to maintain the density and temperature profiles at their background values. For these simulations, some transport characteristics

are quite sensitive to the amplitude of these source terms. When the sources are relatively weak, the background electron temperature profile is locally relaxed by the MTMs, thereby stabilizing the mode. As the modes are stabilized due to the relaxed background gradients, the sources are then capable of restoring the background profiles at a rate dependent on the strength of the source coefficients and the instability grows once again. This results in the cyclical behavior shown in Fig. 7 A. If the sources are increased beyond a certain threshold, the decay does not occur, but the simulations end in numerical instability after a very brief saturation period. Even when the sources are low, the simulations often end in numerical instability, as is seen in Fig. 7 A. for both the blue and red time traces. Despite the sensitivity of the time traces to the source terms, other features of the simulations appear to be quite resilient to the details of the sources. Notably, the peak of the heat flux is rather insensitive to the value of the sources, and is at a level that is quite close to the inter-ELM power loss, as seen in Fig. 7 B., where the radial profile of the electromagnetic heat flux is shown averaged over different time periods.

The nonlinear modification to the background temperature gradient a/L_{Te} is shown in Fig. 7 C. for two time periods, showing a strong localized flattening of the temperature profile along with increases in the gradient on either side of the island region. Despite the large localized change in gradients, the profile itself stays clearly within the uncertainties of the profile fit (recall Fig. 1). Assuming a statistical quasi-steady state, the outward radial heat flux from all transport mechanisms should be roughly constant across the domain. Simulations of electron temperature gradient (ETG) transport for this discharge are reported in Ref. [28] and produced transport levels of $1-4MW$ in the pedestal depending on radial location, suggesting it as the most likely mechanism responsible for the remaining electron heat transport. For reference, the ETG simulation located at $\rho_{tor} = 0.975$ is closest to the MTM location ($\rho_{tor} = 0.978$) and produces 4 MW of electron heat transport. In the actual physical system, MTMs and ETG are likely to vigorously interact, with, for example, MTMs working to flatten the temperature profile and ETG strongly stimulated in the steep gradient regions on either side of the island (see Fig. 7 C.) acting to reinforce the temperature gradient in the flattened region. See Refs. [42, 43] for additional work on multiscale interaction between MTMs and ETG.

The frequency spectrum from the nonlinear simulation is shown in Fig. 8 resolved in toroidal mode number. The precise values of the nonlinear frequencies are dependent on which phase of the nonlinear simulation is analyzed since the MTM frequency is very close to ω_*, which decreases as the profiles relax. The frequency spectrum shown in the figure is calculated over the time period of peak heat flux $t(a/c_s) = 73-83$ and produces frequencies that are quite close to the experimental bands (see the red lines in Fig. 2 and red stars in Fig. 3). The frequency downshift is due to the relaxed background electron temperature gradient (i.e. a reduction in ω_{e*}) that develops over the course of the simulation (recall Fig. 7 C.). Averaging over the time period $t(a/c_s) = 83-93$ results in an even larger reduction in the nonlinear frequencies (not shown).

We emphasize the close agreement between simulation and experiment exhibited in

Fig. 8. With modest variations of input parameters within experimental uncertainties, the simulations capture multiple features of the experimentally observed magnetic fluctuations, including the width and peaks of the magnetic fluctuation frequencies along with their corresponding toroidal mode numbers. We note that such specific experimental observations are much more difficult to reproduce via simulation than a coarse-grained quantity like heat flux.

6. Discussion of inter-ELM Pedestal Dynamics

In the context of the results described above, we propose a picture of the role of MTMs in the inter-ELM evolution of the pedestal. Following an ELM crash, the temperature and density profiles rebuild at different rates [44, 3, 4, 45] and likely mediated by different transport mechanisms [26, 46]. In the context of MTM activity, we are particularly interested in the rebuilding of the electron temperature profile, which will steepen until the MTM surpasses some threshold. The stability threshold will be crossed first at the radial location of peak drive (i.e. peak in ω_*) and at toroidal mode numbers where two criteria are satisfied: (1) the collision frequency and mode frequency are sufficiently close $\nu \approx \omega_*$ (or more precisely, the MTM dispersion relation produces instability), and (2) the relevant rational surface aligns with the peak in ω_*. The latter criterion is particularly relevant in pedestals with low magnetic shear and/or where MTMs are stimulated at low toroidal mode number where rational surfaces are more sparse. In such scenarios, MTMs will be unstable at disparate n numbers, as is often observed in magnetic spectrograms, the present study being representative. In other scenarios where the resonance occurs at higher n or where magnetic shear is sufficiently high to produce a continuum of MTM instability, MTMs will likely be manifest as a broader band of fluctuations over a range of consecutive n numbers, as is reported in Ref. [1].

The propensity of MTMs to arise at the peak in the ω_* profile is likely to set an upper bound on the maximum temperature gradient accessible in a given pedestal scenario. Once MTMs sufficiently surpass their linear threshold, they form magnetic islands and rapidly relax the background electron temperature profile in a region surrounding the rational surface. ETG transport is likely to be closely linked to these dynamics as follows. The flattening of the background temperature profile will simultaneously create localized regions of steep temperature gradients at the boundaries of the islands (see Fig. 7), which will in turn produce fine-scale ETG turbulence in these regions. Other interaction between MTMs and ETG is also possible, for example, direct nonlinear coupling between scales and/or the interaction of both with background flows and fields. Direct coupling may be rather unlikely considering the distinct poloidal locations at which each transport mechanism operates, with MTMs favoring the top/bottom of the tokamak and ETG favoring the outboard midplane as shown in Fig. 9. Interaction with lower n toroidal ETG modes [47] is also an important consideration. These fascinating multi-scale interactions are the topic of ongoing study with an initial investigation reported in Ref. [42]. Earlier work for core-like parameters is reported in Ref. [43].

ETG is also the most likely candidate to account for electron heat transport across the regions of the pedestal not limited by MTMs.

Other transport channels (impurities, ion temperature, density) are mediated by separate transport mechanisms as described in detail in [26, 46].

7. Discussion and Conclusions

This paper describes a theoretical and numerical examination of magnetic fluctuations observed in the JET pedestal, unambiguously identifying them as MTMs. Gyrokinetic simulations quantitatively capture many distinctive features of the experimentally observed fluctuations, including the width, peaks, and toroidal mode numbers associated with two prominent frequency bands observed in magnetic spectrograms. A major achievement of this work is a clear explanation for the discrete bands observed at disparate toroidal mode numbers $n = 4, 8$. This distinctive feature of the fluctuations is due to the alignment of the $n = 4, 8$ rational surfaces with the peak in the ω_* profile and the misalignment of the rational surface corresponding to the other n numbers. Comparisons with a simple MTM dispersion relation were shown, exhibiting good agreement on the collisionality threshold and qualitative agreement on the growth rate dependence on collision frequency. Although some modes were found to have collisionless tails where MTMs remain unstable, the experimental points lie in the collisional or semi-collisional regimes. Despite some limitations, nonlinear simulations elucidate many aspects of the experimental observations and offer valuable physical insights. The MTMs saturate by relaxing the background temperature gradient. The resulting local reduction brings the frequencies into close agreement with the experimental observations. We posit that ETG and MTMs closely interact to account for electron heat transport across the pedestal. ETG likely serves as the main electron heat transport mechanism in regions of the pedestal outside the MTM region and likely serves to reinforce the background temperature gradient as it is relaxed by MTMs. This paper further establishes the physical basis for the origin, role, and distinctive characteristics of an important and commonly observed pedestal fluctuation.

Acknowledgements.– We would like to thank Florian Laggner for useful discussions. This research used resources of the National Energy Research Scientific Computing Center, a DOE Office of Science User Facility. We acknowledge the CINECA award under the ISCRA initiative, for the availability of high performance computing resources and support. This work was supported by U.S. DOE Contract No. DE-FG02-04ER54742 and U.S. DOE Office of Fusion Energy Sciences Scientific Discovery through Advanced Computing (SciDAC) program under Award Number DE-SC0018429. This work has been carried out within the framework of the EUROfusion Consortium and has received funding from the Euratom research and training programme 2014-2018 and 2019-2020 under grant agreement No 633053. The views and opinions expressed herein do not necessarily reflect those of the European Commission.

Appendix A. Treatment of $E \times B$ and Doppler Shift

Consider the Doppler shift due to a radial electric field E_r. The poloidal and toroidal velocity associated with this satisfy the radial component of $E + v \times B = 0$:

$$E_r + v_{pol} B_{tor} - v_{tor} B_{pol} = 0 \tag{A.1}$$

The Doppler shift will be

$$\mathbf{k} \cdot \mathbf{v} = k_{pol} v_{pol} + k_{tor} v_{tor} \tag{A.2}$$

Tokamak instabilities are characterized by $\mathbf{k} \cdot \mathbf{B} = 0$, which becomes

$$k_{pol} B_{pol} + k_{tor} B_{tor} = 0 \tag{A.3}$$

Using Eq. A.3 to eliminate k_{pol} in Eq. A.2, we get:

$$\omega_{Doppler} = -k_{tor} v_{pol} \frac{B_{tor}}{B_{pol}} + k_{tor} v_{tor} = -\frac{k_{tor}}{B_{pol}} (v_{pol} B_{tor} - v_{tor} B_{pol}) \tag{A.4}$$

Using Eq. A.1, this becomes

$$\omega_{Doppler} = \frac{k_{tor} E_r}{B_{pol}} = \frac{n E_r}{R B_{pol}} \tag{A.5}$$

where the final expression uses $k_{tor} = n/R$.

The Doppler shift is as if the velocity is totally in the toroidal direction. Any combination of poloidal and toroidal velocity satisfying Eq. A.1, regardless of the distribution in the poloidal and toroidal direction, will result in Eq. A.5. By eliminating k_{tor} in Eq. A.3, we could equally well arrive at:

$$\omega_{Doppler} = \frac{k_{pol} E_r}{B_{tor}} \tag{A.6}$$

Note that the neoclassical force balance equation defined in Eq. 1 expresses the radial electric field as $\frac{d\Phi_0}{d\psi} = \frac{\nabla \Phi_0}{\nabla \psi} = \frac{E_r}{R B_{pol}}$. Furthermore, the GENE code is spectral in the binormal, $k_y \propto n$, direction. Consequently, the use of toroidal rotation is convenient, and the $E \times B$ rotation is included as toroidal rotation as defined in Eq. A.5.

Appendix B. How to calculate ω_*

Below I outline how to calculate ω_* from (1) GENE data (k_y, omn, and omt), experimental data expressed in terms of toroidal mode number n and (2) radial coordinate ρ_{tor}, (3) radial coordinate ψ, and (4) radial coordinate r. These calculations should be made at the radial location where ω_* peaks in the pedestal.

$$\omega_* = k_y \rho_s c_s \left(\frac{1}{L_n} + \frac{1}{L_{Te}} \right) = \frac{\rho_s}{a} \frac{c_s}{a} \frac{qn}{\rho_{tor}} \left(\frac{dn_0}{n_0 d\rho_{tor}} + \frac{dT}{T d\rho_{tor}} \right) \tag{B.1}$$

In this expression the binormal wavenumber, k_y is related to the toroidal mode number n as

$$k_y \rho_s = \frac{\rho_s q}{\rho_{tor} a} n \tag{B.2}$$

where ρ_s is the sound gyro radius, q is the safety factor, a is the minor radius, and $\rho_{tor} = \Phi_N^{1/2}$ is the square root of the normalized toroidal magnetic flux. The gradient scale lengths are defined as $\frac{a}{L_n} = \frac{1}{n_0}\frac{dn_0}{d\rho_{tor}}$ and likewise for T (using n_0 to denote density as opposed to toroidal mode number).

We will convert the above expression for ω_* into derivatives with respect to poloidal flux ψ. Note that

$$\frac{d\rho_{tor}}{d\psi_N} = \frac{1}{2}\Phi_N^{-1/2}\frac{d\Phi_N}{d\psi_N} = \frac{q}{2\rho_{tor}}\frac{\psi_{sep}}{\Phi_{sep}} \tag{B.3}$$

using $\frac{d\Phi}{d\psi} = q$, where Φ_N and ψ_N are the toroidal flux Φ and poloidal flux ψ normalized to their separatrix values Φ_{sep} and ψ_{sep}, respectively.

Using Eqs. B.2 and B.3,

$$\omega_* = \frac{\rho_s q}{\rho_{tor} a} n \frac{c_s}{a}\left(\frac{1}{n_0}\frac{dn_0}{d\psi_N} + \frac{1}{T}\frac{dT}{d\psi_N}\right)\frac{d\psi}{d\rho_{tor}} \tag{B.4}$$

$$= \frac{\Phi_{sep}}{\psi_{sep}}\frac{2\rho_s c_s}{a^2} n \left(\frac{1}{n_0}\frac{dn_0}{d\psi_N} + \frac{1}{T}\frac{dT}{d\psi_N}\right) \tag{B.5}$$

$$= \frac{\Phi_{sep}}{\psi_{sep}} n \frac{2T_e}{a^2 e B_0}\left(\frac{1}{n_0}\frac{dn_0}{d\psi_N} + \frac{1}{T}\frac{dT}{d\psi_N}\right) \tag{B.6}$$

We can further translate to the minor radius (in meters) radial coordinate (note that ψ is now un-normalized):

$$\omega_* = n\left(\frac{\Phi_{sep}}{a^2 B_0}\right)\frac{2T_e}{e}\left(\frac{1}{n_0}\frac{dn_0}{d\psi} + \frac{1}{T}\frac{dT}{d\psi}\right) \tag{B.7}$$

$$= n\left(\frac{\Phi_{sep}}{a^2 B_0}\right)\frac{2T_e}{e}\left(\frac{1}{n_0}\frac{\nabla n_0}{\nabla\psi} + \frac{1}{T}\frac{\nabla T}{\nabla\psi}\right) \tag{B.8}$$

$$= n\left(\frac{\Phi_{sep}}{a^2 B_0}\right)\frac{2T_e}{eRB_\theta}\left(\frac{\nabla n_0}{n_0} + \frac{\nabla T}{T}\right) \tag{B.9}$$

Appendix C. Numerical setup of gyrokinetic simulations

This work used the GENE code mostly in its global mode of operation. Numerical details of the simulations are described in this appendix. All simulations were electromagnetic and employed a Landau-Boltzmann collision operator [48] with collision frequencies defined by the experimental conditions. All global simulations include background $E \times B$ shear. The recently-developed block-structured velocity space grids [49, 50] were exploited to reduce the demands on velocity space resolution, accelerating global simulations.

Global simulations use 320 radial grid points and span the domain $\rho_{tor} = 0.94 - 0.995$. Dirichlet boundary conditions were enforced at the radial boundaries and

transition regions were implemented (10 % on each side) over which gradients are smoothly set to zero and Krook damping smoothly ramps up to set fluctuations to zero at the boundary.

In the parallel z direction, $60 - 64$ grid points were employed. In parallel velocity $v_{||}$, and magnetic moment μ coordinates (i.e. squared perpendicular velocity), $(60, 24)$ grid points were used, respectively, in the absence of block-structured grids. This could be reduced to $(\sim 36, 12)$ when block-structured grids were employed. The parallel domain was from $-\pi$ to π (poloidal angle), and the velocity space domains are adapted radially to span approximately -3 to 3 in the parallel velocity coordinate (normalized to $\sqrt{T_e/m_i}$), and 0 to 9 (normalized to T_e/B_0) in the μ coordinate. In the block-structured grids approach, these domains are adapted radially corresponding to the local temperatures. Source rates ranging from 0.05 to 0.5 were tested in the nonlinear simulations. Values above 0.35 generally prevented the relaxation of the background gradients but resulted in numerical instabilities early in the simulations. Values in the range 0.1-0.2 were used for the simulations shown in Fig. 7, for which the background gradients relaxed and subsequently rebuilt.

Fourth order hyperdiffusion [51] was employed in the parallel, radial, and parallel velocity coordinates. Coefficients in the radial direction range from 2-10, in the parallel velocity direction 0.2, and in the parallel direction the coefficient was set to the corresponding value for an upwinding scheme.

Appendix D. References

[1] C. P. Perez, H. R. Koslowski, T. C. Hender, P. Smeulders, A. Loarte, P. J. Lomas, G. Saibene, R. Sartori, M. Becoulet, T. Eich, and others. Washboard modes as ELM-related events in JET. *Plasma physics and controlled fusion*, 46(1):61, 2003.

[2] A. Diallo, J. W. Hughes, M. Greenwald, B. LaBombard, E. Davis, S-G. Baek, C. Theiler, P. Snyder, J. Canik, J. Walk, T. Golfinopoulos, J. Terry, M. Churchill, A. Hubbard, M. Porkolab, L. Delgado-Aparicio, M. L. Reinke, A. White, and Alcator C-Mod team. Observation of edge instability limiting the pedestal growth in tokamak plasmas. *Phys. Rev. Lett.*, 112:115001, Mar 2014.

[3] A. Diallo, R. J. Groebner, T. L. Rhodes, D. J. Battaglia, D. R. Smith, T. H. Osborne, J. M. Canik, W. Guttenfelder, and P. B. Snyder. Correlations between quasi-coherent fluctuations and the pedestal evolution during the inter-edge localized modes phase on diii-d. *Physics of Plasmas*, 22(5):056111, 2015.

[4] F. M. Laggner, E. Wolfrum, M. Cavedon, F. Mink, E. Viezzer, M. G. Dunne, P. Manz, H. Doerk, G. Birkenmeier, R. Fischer, S Fietz, M. Maraschek, M. Willensdorfer, F. Aumayr, the EUROfusion MST1 Team, and the ASDEX Upgrade Team. High frequency magnetic fluctuations correlated with the inter-ELM pedestal evolution in ASDEX Upgrade. *Plasma Physics and Controlled Fusion*, 58(6):065005, 2016.

[5] M. Cavedon, R. Dux, T. Ptterich, E. Viezzer, E. Wolfrum, M. Dunne, E. Fable, R. Fischer, G.F. Harrer, F.M. Laggner, A.F. Mink, U. Plank, U. Stroth, M. Willensdorfer, and Asdex Upgrade Team. On the ion and electron temperature recovery after the ELM-crash at ASDEX upgrade. *Nuclear Materials and Energy*, 18:275–280, January 2019.

[6] Jie Chen, David Brower, Weixing Ding, Zheng Yan, Tom Osborne, E Strait, Max Curie, David Hatch, Michael Kotschenreuther, Xiang Jian, M. Halfmoon, and Swadesh Mahajan. Internal

measurement of magnetic turbulence in elmy h-mode tokamak plasmas, in publication. *Physics of Plasmas*.

[7] F.M. Laggner, A. Diallo, M. Cavedon, and E. Kolemen. Inter-elm pedestal localized fluctuations in tokamaks: Summary of multi-machine observations. *Nuclear Materials and Energy*, 19:479 – 486, 2019.

[8] F. Jenko, W. Dorland, M. Kotschenreuther, and B.N. Rogers. Electron temperature gradient driven turbulence. *Phys. Plasmas*, 7:1904, 2000.

[9] T. Görler, X. Lapillonne, S. Brunner, T. Dannert, F. Jenko, F. Merz, and D. Told. The global version of the gyrokinetic turbulence code GENE. *Journal of Computational Physics*, 230(18):7053–7071, August 2011.

[10] R. D. Hazeltine, D. Dobrott, and T. S. Wang. Kinetic theory of tearing instability. *Phys. Fluids*, 18(12):1778, 1975.

[11] Swadesh M. Mahajan, R. D. Hazeltine, H. R. Strauss, and David W. Ross. Unified theory of tearing modes. *The Physics of Fluids*, 22(11):2147–2157, 1979.

[12] N. T. Gladd, J. F. Drake, C. L. Chang, and C. S. Liu. Electron temperature gradient driven microtearing mode. *Phys. Fluids*, 23(6):1182, 1980.

[13] D. Carmody, M. J. Pueschel, and P. W. Terry. Gyrokinetic studies of microinstabilities in the reversed field pinch. *Physics of Plasmas*, 20(5):052110, 2013.

[14] I. Predebon and F. Sattin. On the linear stability of collisionless microtearing modes. *Physics of Plasmas*, 20(4):040701–040701–4, April 2013.

[15] Aditya K. Swamy, R. Ganesh, J. Chowdhury, S. Brunner, J. Vaclavik, and L. Villard. Global gyrokinetic stability of collisionless microtearing modes in large aspect ratio tokamaks. *Physics of Plasmas*, 21(8):082513, 2014.

[16] M. Hamed, M. Muraglia, Y. Camenen, and X. Garbet. Stability of a slab collisional microtearing mode. *Contributions to Plasma Physics*, 58(6-8):529–533.

[17] H. Doerk, F. Jenko, M. J. Pueschel, and D. R. Hatch. Gyrokinetic Microtearing Turbulence. *Physical Review Letters*, 106(15), April 2011.

[18] H. Doerk, F. Jenko, T. Grler, D. Told, M. J. Pueschel, and D. R. Hatch. Gyrokinetic prediction of microtearing turbulence in standard tokamaks. *Physics of Plasmas*, 19(5):055907, 2012.

[19] W. Guttenfelder, J. Candy, S. M. Kaye, W. M. Nevins, E. Wang, R. E. Bell, G. W. Hammett, B. P. LeBlanc, D. R. Mikkelsen, and H. Yuh. Electromagnetic Transport from Microtearing Mode Turbulence. *Phys. Rev. Lett.*, 106(15):155004, April 2011.

[20] D J Applegate, C M Roach, J W Connor, S C Cowley, W Dorland, R J Hastie, and N Joiner. Micro-tearing modes in the mega ampere spherical tokamak. *Plasma Physics and Controlled Fusion*, 49(8):1113, 2007.

[21] J. Chowdhury, Yang Chen, Weigang Wan, Scott E. Parker, W. Guttenfelder, and J. M. Canik. Particle-in-cell f gyrokinetic simulations of the microtearing mode. *Physics of Plasmas (1994-present)*, 23(1):012513, January 2016.

[22] D. Dickinson, C. M. Roach, S. Saarelma, R. Scannell, A. Kirk, and H. R. Wilson. Kinetic instabilities that limit β in the edge of a tokamak plasma: A picture of an h-mode pedestal. *Phys. Rev. Lett.*, 108:135002, Mar 2012.

[23] J.M. Canik, W. Guttenfelder, R. Maingi, T.H. Osborne, S. Kubota, Y. Ren, R.E. Bell, H.W. Kugel, B.P. LeBlanc, and V.A. Souhkanovskii. Edge microstability of nstx plasmas without and with lithium-coated plasma-facing components. *Nuclear Fusion*, 53(11):113016, 2013.

[24] X. Jian, C. Holland, J. Candy, E. Belli, V. Chan, A.M. Garofalo, and S. Ding. Role of Microtearing Turbulence in DIII-D High Bootstrap Current Fraction Plasmas. *Phys. Rev. Lett.*, 123(22):225002, November 2019.

[25] D. R. Hatch, M. Kotschenreuther, S. Mahajan, P. Valanju, F. Jenko, D. Told, T. Görler, and S. Saarelma. Microtearing turbulence limiting the JET-ILW pedestal. *Nuclear Fusion*, 56(10):104003, 2016.

[26] M. Kotschenreuther, X. Liu, D.R. Hatch, S. Mahajan, L. Zheng, A. Diallo, R. Groebner, the DIII-

D TEAM, J.C. Hillesheim, C.F. Maggi, C. Giroud, F. Koechl, V. Parail, S. Saarelma, E. Solano, A. Chankin, and JET Contributors. Gyrokinetic analysis and simulation of pedestals to identify the culprits for energy losses using fingerprints. *Nucl. Fusion*, 59(9):096001, September 2019.

[27] J. Chen, W. X. Ding, D. L. Brower, D. Finkenthal, C. Muscatello, D. Taussig, and R. Boivin. Faraday-effect polarimeter diagnostic for internal magnetic field fluctuation measurements in diii-d. *Review of Scientific Instruments*, 87(11):11E108, 2016.

[28] D.R. Hatch, M. Kotschenreuther, S.M. Mahajan, G. Merlo, A.R. Field, C. Giroud, J.C. Hillesheim, C.F. Maggi, C. Perez von Thun, C.M. Roach, S. Saarelma, and JET Contributors. Direct gyrokinetic comparison of pedestal transport in JET with carbon and ITER-like walls. *Nucl. Fusion*, 59(8):086056, August 2019.

[29] Matt Landreman and Darin R Ernst. Local and global fokkerplanck neoclassical calculations showing flow and bootstrap current modification in a pedestal. *Plasma Physics and Controlled Fusion*, 54(11):115006, 2012.

[30] E. Viezzer, T. Ptterich, G.D. Conway, R. Dux, T. Happel, J.C. Fuchs, R.M. McDermott, F. Ryter, B. Sieglin, W. Suttrop, M. Willensdorfer, E. Wolfrum, and the ASDEX Upgrade Team. High-accuracy characterization of the edge radial electric field at asdex upgrade. *Nuclear Fusion*, 53(5):053005, 2013.

[31] D Dickinson, C M Roach, S Saarelma, R Scannell, A Kirk, and H R Wilson. Microtearing modes at the top of the pedestal. *Plasma Physics and Controlled Fusion*, 55(7):074006, 2013.

[32] S. Saarelma, M.N.A. Beurskens, D. Dickinson, L. Frassinetti, M.J. Leyland, C.M. Roach, and EFDA-JET Contributors. Mhd and gyro-kinetic stability of jet pedestals. *Nuclear Fusion*, 53(12):123012, 2013.

[33] R.J. Hastie and K.W. Hesketh. Kinetic modifications to the MHD ballooning mode. *Nuclear Fusion*, 21(6):651–656, jun 1981.

[34] C. Z. Cheng. Kinetic theory of collisionless ballooning modes. *The Physics of Fluids*, 25(6):1020–1026, 1982.

[35] M. Kotschenreuther. Compressibility effects on ideal and kinetic ballooning modes and elimination of finite larmor radius stabilization. *The Physics of Fluids*, 29(9):2898–2913, 1986.

[36] Felix I Parra and Michael Barnes. Equivalence of two different approaches to global delta f gyrokinetic simulations. *Plasma Physics and Controlled Fusion*, 57(5):054003, apr 2015.

[37] P A Abdoul, D Dickinson, C M Roach, and H R Wilson. Using a local gyrokinetic code to study global ion temperature gradient modes in tokamaks. *Plasma Physics and Controlled Fusion*, 57(6):065004, apr 2015.

[38] A R Field, C D Challis, J M Fontdecaba, L Frassinetti, L Horvath, Hyun-Tae Kim, C Maggi, C M Roach, S Saarelma, M Sertoli, and G Szepeisi and. The dependence of exhaust power components on edge gradients in JET-c and JET-ILW h-mode plasmas. *Plasma Physics and Controlled Fusion*, 62(5):055010, mar 2020.

[39] J. L. Larakers, R. D. Hazeltine, and S. M. Mahajan. A comprehensive conductivity model for drift and micro-tearing modes. *Physics of Plasmas*, 27(6):062503, 2020.

[40] M. Hamed, M. Muraglia, Y. Camenen, X. Garbet, and O. Agullo. Impact of electric potential and magnetic drift on microtearing modes stability. *Physics of Plasmas*, 26(9):092506, 2019.

[41] E. Hassan, D. R. Hatch, M. Halfmoon, G Merlo, A. O. Nelson, M. Kotschenreuther, S. Mahajan, R. J. Groebner, and A. Diallo. Clear signature of micro-tearing modes in the diii-d pedestal. *in preparation*.

[42] M.J. Pueschel, D.R. Hatch, M. Kotschenreuther, A. Ishizawa, and G. Merlo. Multi-scale interactions of microtearing turbulence in the tokamak pedestal. *Nucl. Fusion*, 60(12):124005, December 2020.

[43] S. Maeyama, T.-H. Watanabe, and A. Ishizawa. Suppression of Ion-Scale Microtearing Modes by Electron-Scale Turbulence via Cross-Scale Nonlinear Interactions in Tokamak Plasmas. *Physical Review Letters*, 119(19), November 2017.

[44] E. Wolfrum, A. Burckhart, R. Fischer, N. Hicks, C. Konz, B. Kurzan, B. Langer, T. Ptterich,

H. Zohm, and the ASDEX Upgrade Team. Investigation of inter-ELM pedestal profiles in ASDEX Upgrade. *Plasma Phys. Control. Fusion*, 51(12):124057, December 2009.

[45] C.F. Maggi, L. Frassinetti, L. Horvath, A. Lunniss, S. Saarelma, H. Wilson, J. Flanagan, M. Leyland, I. Lupelli, S. Pamela, H. Urano, L. Garzotti, E. Lerche, I. Nunes, F. Rimini, and JET Contributors. Studies of the pedestal structure and inter-elm pedestal evolution in jet with the iter-like wall. *Nuclear Fusion*, 57(11):116012, 2017.

[46] D. R. Hatch and *et al.* Final report for the fy19 fes theory performance target. Technical report, 2019.

[47] Jason F. Parisi, Felix I. Parra, Colin M. Roach, Carine Giroud, William Dorland, David R. Hatch, Michael Barnes, Jon C. Hillesheim, Nobuyuki Aiba, Justin Ball, Plamen G. Ivanov, and JET Contributors. Toroidal and slab etg instability dominance in the linear spectrum of jet-ilw pedestals, 2020.

[48] H. Doerk. Gyrokinetic simulation of microtearing turbulence. *Dissertation, University of Ulm*, 2013.

[49] D. Jarema, H. J. Bungartz, T. Grler, F. Jenko, T. Neckel, and D. Told. Block-structured grids for Eulerian gyrokinetic simulations. *Computer Physics Communications*, 198:105–117, January 2016.

[50] D. Jarema, H. J. Bungartz, T. Grler, F. Jenko, T. Neckel, and D. Told. Block-structured grids in full velocity space for Eulerian gyrokinetic simulations. *Computer Physics Communications*, 215:49 – 62, 2017.

[51] M.J. Pueschel, T. Dannert, and F. Jenko. On the role of numerical dissipation in gyrokinetic Vlasov simulations of plasma microturbulence. *Computer Physics Communications*, 181(8):1428–1437, August 2010.

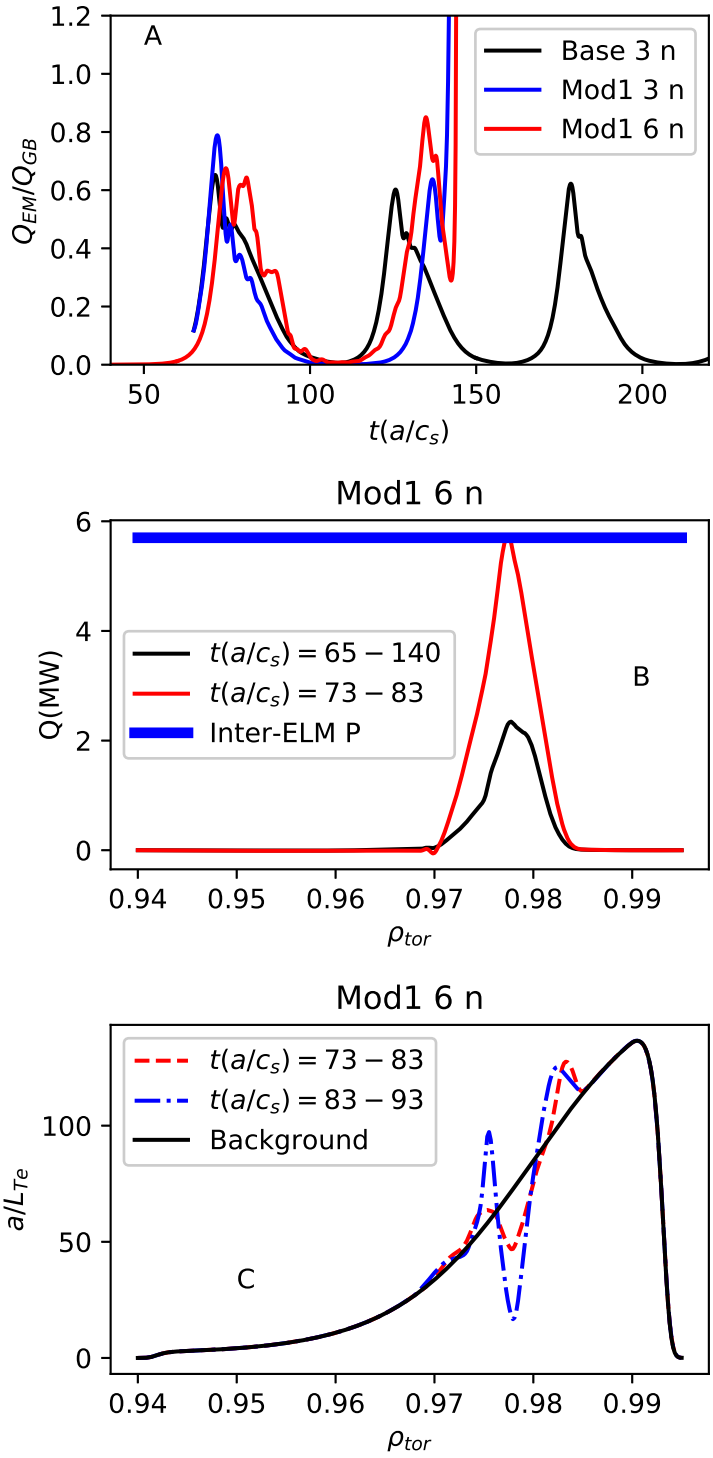

Figure 7. Time traces of electromagnetic heat flux (A.) for three simulations: the Base case with three toroidal mode numbers ($n = 0, 4, 8$), the Mod 1 case with three toroidal mode numbers ($n = 0, 4, 8$), and the Mod 1 case with six toroidal mode numbers ($n = 0, 2, 4, 6, 8, 10$). This simulation with six modes is used for plots B. and C. The latter two simulations end in numerical instabilities at $t(a/c_s) \sim 145$. The radial profile of the electromagnetic heat flux (B.) averaged over two different time periods. The radial profile of a/L_{Te}, demonstrating that the mode saturates by relaxing the background temperature gradient (C.).

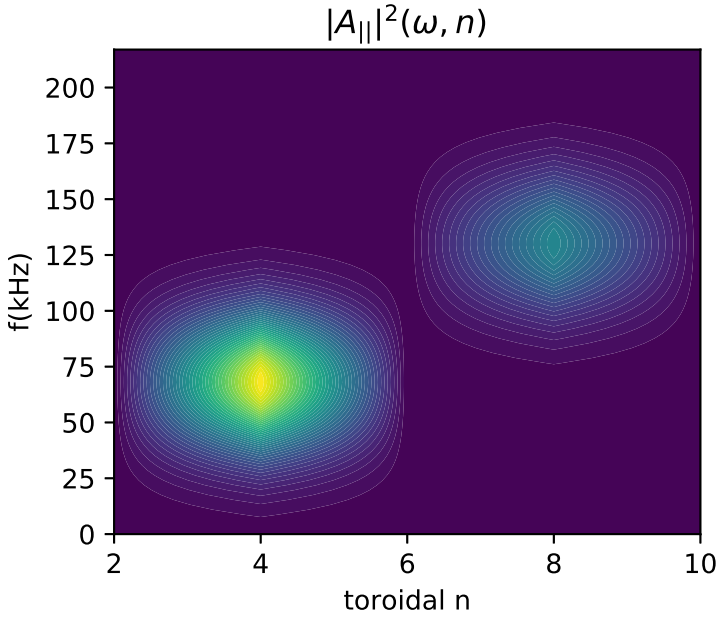

Figure 8. The frequency spectrum calculated during $t(a/c_s) = 73-83$ of the six mode nonlinear simulation. This spectrum agrees closely with the n numbers and frequency bands in the magnetic spectrogram (Fig. 2).

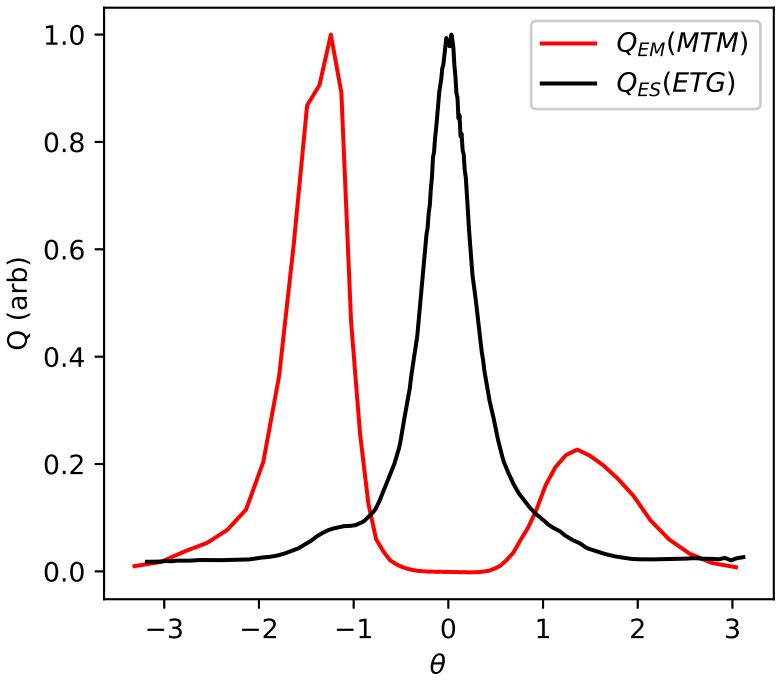

Figure 9. Poloidal distribution of heat flux from MTMs (red) and ETG (black). The MTM simulation is global and limited to low k_y, whereas the ETG simulation produces heat flux at very small scales ($k_y\rho_s \approx 80$). For reference, the ETG simulation is a local simulation at $\rho_{tor} = 0.975$ and produces 4 MW of transport.